

1 **Title page**

2

3 **Iron colloids dominate sedimentary supply to the**
4 **ocean interior**

5

6

7

8 William B Homoky^{ab1}, Tim M Conway^c, Seth G John^d, Daniela Koenig^e, FeiFei
9 Deng^b, Alessandro Tagliabue^e, Rachel A. Mills^f

10

11 ^aUniversity of Leeds, School of Earth and Environment, UK

12 ^bUniversity of Oxford, Department of Earth Sciences, UK

13 ^cUniversity of South Florida, College of Marine Science, USA

14 ^dUniversity of Southern California, Department of Earth Sciences, USA

15 ^eUniversity of Liverpool, School of Environmental Sciences, UK

16 ^fUniversity of Southampton, School of Ocean and Earth Science, UK

17

18

19 ¹ To whom correspondence should be addressed. Email: W.Homoky@leeds.ac.uk

20

21

22

23

24

25 **Abstract**

26 Dissolution of marine sediment is a key source of dissolved iron (Fe) that
27 regulates the ocean carbon cycle. Currently, our prevailing understanding,
28 encapsulated in ocean models, focuses on low oxygen reductive supply
29 mechanisms and neglects the emerging evidence from iron isotopes in
30 seawater and sediment porewaters for additional non-reductive dissolution
31 processes. Here we combine new measurements of Fe colloids and dissolved
32 $\delta^{56}\text{Fe}$ in shallow porewaters spanning the full depth of the South Atlantic
33 Ocean to demonstrate that it is lithogenic colloid production that fuels
34 sedimentary iron supply away from low oxygen systems. Iron colloids are
35 ubiquitous in these oxic ocean sediment porewaters and account for the
36 lithogenic isotope signature of dissolved Fe ($\delta^{56}\text{Fe} = +0.07 \pm 0.07\%$) within and
37 between ocean basins. Isotope model experiments demonstrate that only
38 lithogenic weathering in both oxic and nitrogenous zones, rather
39 than precipitation or ligand-complexation of reduced Fe species, can account
40 for the production of these pore water Fe colloids. The broader covariance
41 between colloidal Fe and organic carbon (OC) abundance suggests that
42 sorption of OC may control the nano-scale stability of Fe minerals by inhibiting
43 loss of Fe(oxyhydr)oxides to more crystalline minerals in the sediment. Oxic
44 ocean sediments can therefore generate a large exchangeable reservoir of
45 organo-mineral Fe colloids at the sediment water interface (a “rusty source”)
46 that dominates benthic supply of dissolved Fe to the ocean interior, alongside
47 reductive supply pathways from shallower continental margins.

48 **Keywords:** ocean sediment; porewater; iron isotope; iron colloid; iron organo-
49 mineral

50

51

52

53 **Significance statement**

54 Phytoplankton assimilate carbon dioxide, produce oxygen and nourish food
55 webs on a scale that impacts planetary processes but are limited by iron
56 deficiency over much of the global surface ocean. Therefore, we must
57 understand processes that regulate the ocean's iron inventory to accurately
58 simulate and predict the ocean's response to change. This study reveals that
59 the widespread production of nano-sized iron colloids from the weathering of
60 lithogenic material drives sedimentary iron supply throughout the deep ocean.
61 The discovery accounts for the unexplained occurrence of colloids and
62 patterns of iron isotope variation previously observed in other parts of the
63 deep ocean, and suggests how long standing assumptions we have used to
64 simulate iron supply in ocean models must be revised.

65

66 **Introduction**

67

68 Sediments undergo early diagenetic transformations that are understood to provide an
69 important source of dissolved iron (dFe) to the ocean that is used to fuel primary production
70 and secondary food webs, fix nitrogen and support the air-sea transfer of carbon dioxide (1, 2).
71 Nevertheless, fundamental questions remain concerning the magnitude of dFe released from
72 ocean sediments, and the mechanisms through which this supply may be moderated. Such
73 uncertainty is most acute in oxic and deep-water regions, which bear the fewest observations,
74 but represent the largest area of the ocean sediment-water interface (3). Here, comparatively
75 small sedimentary releases of dFe have the cumulative-potential to enhance the dFe inventory
76 of the deep ocean and – in so far as it connects with surface water – relieve iron-deficiency for
77 phytoplankton. Porewaters in these deep water regions maintain a persistently oxic and/or
78 nitrogenous state adjacent to bottom waters that is largely unexamined for its role in the marine
79 iron cycle. These gaps in knowledge hinder our ability to make more accurate simulations of
80 the carbon cycle in ocean biogeochemical models (4).

81 Two principle processes are thought to be driving Fe dissolution from sediments that
82 underpin the magnitude and variability of dFe inputs to the ocean. The first is a reductive-
83 dissolution (RD) process which demonstrably occurs during early diagenetic oxidation of
84 organic carbon (OC) and produces high abundances of reduced, soluble and isotopically light
85 Fe in ferruginous porewaters generally beneath the Fe-oxidising fronts of nitrous oxides and
86 oxygen (5-7). The second is a non-reductive dissolution (NRD) process to account for the
87 comparatively unfractionated or heavy isotope compositions of dFe attributed to sedimentary
88 inputs in some oxygenated regions of the open ocean (8) and in the oxic zones of marine
89 sediment porewaters (9), but the mechanisms governing so-called NRD in oxic sediments are
90 unclear.

91 Reductive dissolution of Fe is coupled to organic carbon oxidation and is widely
92 observed in shallow porewater in sediments with high oxygen consumption rates, under
93 productive shelf seas, near zones of upwelling and overlain by oxygen-depleted seawater (10).
94 Low seawater oxygen content serves to enhance the efflux of reduced and soluble Fe (sFe;
95 filtered $<0.02 \mu\text{m}$) from ferruginous pore waters and enables sFe(II) to propagate further in the
96 water column (11-14). Subsequently, without sufficient chelation by organic ligands sFe(II)

97 will be lost to oxidative precipitation (7, 15, 16) scavenging (12) and sedimentation in deeper
98 water (16, 17). Sedimentary RD provides a key component of the ocean's dFe inventory that is
99 most pronounced in the upper ocean (1, 10, 11, 13). It is also the only mechanism by which
100 most ocean biogeochemical models simulate the sedimentary release of dFe (4), since model
101 parameterisations rely on empirical relationships between dFe fluxes, OC oxidation rates,
102 bottom water oxygen contents, and/or water depth (1, 11, 18, 19).

103 Non-reductive dissolution (NRD) is a term previously used to describe a sedimentary
104 source of isotopically heavy dFe to the water column (8), and has since been used to describe
105 the presence of lithogenic isotope compositions observed in oxidizing zones from some deep
106 ocean sediment porewaters (9). Similar observations have become commonplace in the ocean
107 interior (20-23), such that non-reductive sedimentary processes appear to be important for the
108 ocean's dFe inventory. However, the detection of lithogenic dFe isotope signatures in
109 porewaters (6, 9), within western North Atlantic benthic nepheloid layers, and in the water-
110 column far from sediment sources have been difficult to explain (24). The role played by this
111 additional source of dFe is not yet included in global ocean models.

112 Based on the very low solubility of silicate minerals and Fe(III) oxides in circumneutral
113 pH and oxygenated seawater, NRD ought to be incapable of sustaining a benthic flux of dFe
114 to the ocean without significant chelation by organic ligands (25). Due to a strong isotope
115 fractionation effect, however, ligand complexation of Fe would produce a much heavier Fe
116 isotope signal in the ocean (26), which is at odds with the isotopic evidence for NRD (20-23).
117 To reconcile these differences between NRD theories and dissolved Fe isotope observations we
118 ought to consider any physico-chemical partitioning within the dFe pool. The dissolved
119 measurement of Fe (dFe; $<0.2 \mu\text{m}$) and dFe isotopes, may reflect variable contributions of
120 ligand-bound and soluble Fe(II/III) (sFe; $<0.02 \mu\text{m}$) and larger mineral or organo-mineral forms
121 of colloidal Fe (cFe; 0.02 to $0.2 \mu\text{m}$) in the ocean (23, 27). Such components of the dFe pool
122 are often unaccounted for and have been neglected in previous studies reporting the occurrence
123 of sedimentary NRD in the water column. However, sizable concentrations of colloidal Fe (10^1
124 $\mu\text{moles L}^{-1}$) have been observed in oxic-nitrogenous porewaters from deep ocean turbidites of
125 the Southern Ocean, where dFe isotope compositions also matched the solid phase inputs from
126 ocean island basalt. Whether these colloids formed *in situ* through organic complexation, and/or
127 as secondary minerals from either reductive or non-reductive processes was unresolved. A
128 comparison to fresh tephra layers in the Caribbean Sea showed that ocean island basalt
129 weathering and production of nanoscale ferrihydrite or Fe-bearing smectite clays were
130 thermodynamically plausible explanations for cFe in the Southern Ocean porewaters (28).
131 Recently, Klar *et al.*, (7) looked for Fe colloids in porewaters from a shallow shelf sediment,
132 but found few if any, and that the porewaters were dominated by light dFe isotope signatures
133 and sFe(II) attributable to RD by bacteria. Previous studies have not resolved where or why cFe
134 occurs in sediment porewaters of the continental shelf-slope-basin transition, or the extent to
135 which they may influence the inventory and isotope composition of dFe input to the ocean (20,
136 22). These lessons need to be learned by examining the soluble and colloidal partitioning of
137 dissolved Fe in porewaters and comparing them to dissolved Fe isotope signatures from a wider
138 range sedimentary carbon and oxygen regimes in the ocean environment.

139 Without appropriate simulation of this dFe source, ocean biogeochemical models will
140 fail to represent spatial patterns in dFe flux from the seafloor, the response of these fluxes to
141 changing ocean environments, and their consequences for ocean biogeochemistry.
142 Confounding this issue is the omitted role of advective transport mechanisms, internal waves
143 and benthic boundary layers that will facilitate exchanges between oxic sediments and the

144 ocean interior(3, 29, 30). To make progress on this important issue requires new understanding
145 on the mechanisms by which Fe dissolves and is supplied to the ocean by oxic sediments.

146 Herein, we present findings from surface sediment cores from sites that span the depth
147 and breadth of the Southwest Atlantic Ocean. The UK-led GEOTRACES expedition, GA10W,
148 recovered porewaters in 2011 from the Uruguayan continental shelf, slope, Argentine abyssal
149 floor and Mid-Atlantic Ridge (SI Appendix, Table S1). We report porewater dFe isotope
150 compositions and further evidence of the physico-chemical partitioning of dFe between soluble
151 and colloidal size fractions (where $cFe = dFe - sFe$) at selected locations and depths where
152 porewater inventories of Fe were sufficient to permit these determinations. We apply principles
153 of isotope fractionation and mass-balance across the dissolved and soluble size classes to test
154 hypothetical controls on the dFe pool in these porewaters. Our study reveals that oxidizing
155 zones of marine sediments are important regions of non-reductive cFe production derived from
156 lithogenic material, which ultimately determine the dFe inventory and isotope composition
157 supplied to the deep ocean.

158

159 **Results**

160

161 **South Atlantic sediment compositions.** Between the deepest abyssal station of GA10W (18)
162 to the shallowest shelf-top station (24) core top sediments were composed almost entirely of
163 lithogenic material (84 to >99%; Figure 1; averages from 0-5cmbsf, SI Appendix, Table S2) –
164 consistent with continental weathering input and dispersion to the shelf, slopes and abyssal
165 floor of the Argentine Basin (*Cf.* Weijer et al., (31)). Lithogenic material was the second most
166 significant component of core-top material (17%) at the most distal station located on the Mid-
167 Atlantic Ridge, Station 8, more than 3500km from the continental margin along the path of the
168 South Atlantic Current, and above the likely calcite saturation horizon (32). Station 8 was
169 predominantly biogenic carbonate (82%), with trace amounts (<1%) of biogenic opal, whereas
170 stations 18 to 24 contained at most only modest amounts of opal (up to 14%) and carbonate (up
171 to 8%). There was a gradient in total organic carbon (TOC) content from a mid-slope maximum
172 (3.9%, station 22) - coincident with a mid-slope peak in pelagic components - down to
173 minimum values on the permeable sandy shelf (0.2%, station 24) and across the basin on the
174 Mid-Atlantic Ridge (0.2%, station 8).

175

176 **Dissolved porewater contents.** Porewater O_2 was depleted from bottom water values and was
177 observed to penetrate between 0.4 and >9 cm below the seafloor (cmbsf) across all sites. There
178 was a strong exponential relationship between calculated rates of C oxidation (determined from
179 O_2 flux), and water depth (SI Appendix, Fig. S1 and Table S3). Other such indicators of early
180 diagenetic cycling in porewaters had equivalent water depth dependence between stations.

181 Porewater nitrite+nitrate (herein after termed nitrous oxides) were depleted down core
182 from bottom water values (SI Appendix, Fig. S2) and coincided with increased ammonia
183 concentrations (SI Appendix, Table S4). Taken together, these data indicate the reductive
184 cycling of nitrous oxides to ammonia in a nitrogenous zone underlying the oxic surface layer.
185 All stations contained sub-surface maxima in dissolved manganese (dMn) and dFe, up to 10
186 and 52 μM , respectively, consistent with the reductive-dissolution of these metals that has been
187 observed beneath oxic-nitrogenous zones elsewhere in deep-sea sediments (e.g. (9, 33)). A
188 single exception was station 8, where nitrous oxides were not obviously depleted, and where
189 neither dMn nor dFe maxima were observed (SI Appendix Fig. S2 and Table S5).

190 Porewater $\delta^{56}\text{Fe}$ of dFe maxima averaged $-0.93\pm 0.2\%$ (1 SD, $n = 5$) between stations
191 18 and 24 (SI Appendix, Fig. S2), and were isotopically lighter than average igneous crustal
192 material at $\delta^{56}\text{Fe} = +0.09\%$ (34). Light dFe isotopic compositions shifted to heavier values
193 down core and exceeded the average isotopic composition of the crust beneath the ferruginous
194 zones of stations 23 and 22 (up to a maximum of $+0.63\%$). Nearly all stations contained
195 porewater concentrations of dFe in the surface oxic-nitrogenous zones 10 to 500 times higher
196 than background seawater concentrations with $\delta^{56}\text{Fe}$ ($+0.07\pm 0.07\%$, $n = 11$) indistinguishable
197 from average crustal rocks. A single exception was station 23, where ferruginous conditions
198 extended into the upper centimetre of the sediment and a light dFe isotope composition was
199 observed (-1.37%).

200

201 **Soluble and colloidal partitioning of dissolved Fe in porewaters.** A comparison of soluble
202 ($<0.02\mu\text{m}$) and dissolved ($<0.2\mu\text{m}$) porewater filtrates at stations 8, 18, 21 and 22 indicates that
203 sub-surface maxima in dMn and dFe concentration were almost exclusively due to the presence
204 of soluble and most likely reduced species of the metals (Fig. 2; SI Appendix, Table S5; *Cf.*
205 (7)). However, porewater also contained significant detectable quantities of dFe (between 0.01
206 and $0.5\mu\text{M}$) that was far in excess of sFe throughout the overlying nitrogenous and oxic zones.
207 Therefore, between 17 ± 6 and $99\pm 3\%$ of dFe in oxic-nitrogenous porewater was in a colloidal
208 size-class (0.02 to $0.2\mu\text{m}$; Fig. 2). To a lesser but significant extent, dMn also occurred as
209 colloids in the oxic porewater (between 0 and $61\pm 5\%$; SI Appendix, Table S5).

210

211

212 Discussion

213

214 **Early diagenesis of Fe and Mn.** High proportions of lithogenics relative to pelagic material
215 on the Uruguayan margin and deep Argentine Basin compared to the Mid-Atlantic Ridge, (Fig.
216 1) broadly match regional sediment classifications in a recent census of the seafloor, which
217 indicates these sites are also typical of many other margin, basin and ridge environments of the
218 global ocean (35). Calculated fluxes of O_2 in cohesive sediments from the upper shelf slope (St
219 23) to Mid Atlantic Ridge (St 8), and the relationship of these fluxes to water depth (SI
220 Appendix, Fig. S1), follow an expected gradient in the amount of OC that survives
221 remineralisation in the water column and enters the sediment to fuel early diagenetic reactions
222 (36). Porewater properties reported here may therefore provide a suitable analogue for other
223 oxygenated shelf-slope-basin transitions of the global ocean.

224

225 Porewater concentration profiles provide evidence for a common down core sequence
226 of electron acceptor cycling in the order $\text{O}_2 > \text{NO}_x > \text{Mn}^{4+} > \text{Fe}^{3+} > \text{SO}_4^{2-}$, which follows the Gibbs
227 free energy available to the bacteria which catalyse these reduction-oxidation pathways (37).
228 The soluble nature of dFe and dMn maxima (SI Appendix, Fig. S2) is evidence for the reduced
229 species of these metals accumulating in porewaters (*c.f.* (7)). The light isotopic composition of
230 dFe in these ferruginous zones matches previous findings too, where reductive-dissolution of
231 Fe(III)oxyhydroxides to soluble Fe(II)_(aq) was also reasoned to account for similar light $\delta^{56}\text{Fe}$
232 values (5-7, 9, 11, 38, 39), and is supported by experiments (40, 41). However, our novel
233 investigation of the oxic-nitrogenous zones provides evidence for a previously undocumented
234 reservoir of colloidal Fe (cFe) in continental slope and basin sediment porewater of the South
235 Atlantic Ocean (Fig. 2). These colloids will play a crucial role in regional Fe supply, particularly
236 in deep waters, and their occurrence signifies that they are likely to be prevalent in other
oxygenated slope and basin environments.

237

238 **The occurrence of Fe colloids in sediment porewater.** Iron colloids occur commonly in the
239 ocean (23, 27, 42). Most often they are attributed to organic complexation of Fe(III) (43, 44) or
240 nano-particulate Fe(oxyhydr)oxide, clay (45-47) or occasionally Fe sulphide (48) minerals.
241 Recent findings indicate deep Atlantic Ocean waters contain cFe that originates from the
242 seafloor (27), but there are comparatively few assessments of cFe in marine sediment
243 porewaters beyond those presented and discussed in this article (6, 7, 28).

244

Our study shows that the occurrence of cFe in surface sediment porewater is extensive
245 and, thus far, ubiquitous in oxic deep-ocean lithogenic sediments. What is more, these colloids
246 share a nearly identical Fe isotope composition throughout the ocean: in porewaters where dFe
247 has been shown to comprise between 70 and 100% cFe, the dFe isotope composition
248 (+0.12±0.07‰, $n = 24$) remains indistinguishable from the $\delta^{56}\text{Fe}$ of the average igneous
249 weathering product (+0.09‰ (34); Fig. 3). It stands to reason that a common mechanism must
250 be responsible for the formation of cFe from lithogenic material in oxidising environments,
251 which can operate independently of RD driven by bacteria to account for this isotopic
252 uniformity between cFe and lithogenics.

253

The Fe isotope composition of igneous rocks is reflected in its detrital weathering and
254 oxidation product (49, 50). We expect sediments derived from different igneous rocks with
255 different histories of siliciclastic cycling to exhibit variable rates of seafloor weathering,
256 dissolution and authigenesis (3, 9, 51, 52). Accordingly, the porewater content of cFe reported
257 from young deep-ocean Crozet Island Basalt is greater than we report here for the South
258 Atlantic, even for basaltic sites with comparatively low TOC (Fig. 2b). In the present study
259 however, between sites that share a similar lithogenic provenance, we see a strong positive
260 correlation between mean cFe concentration in oxidising porewater and the mean core-top
261 abundance of TOC ($r = 0.962$ $p = 0.04$, $n = 4$; Fig. 2b). Taken together, these igneous and
262 organic relationships reinforce the view that cFe is controlled by the weathering of lithogenic
263 detritus and that OC may be required for the stabilisation of cFe we observe in the porewaters.
264 For example, OC sorption to oxyhydroxide mineral surfaces can inhibit Fe transformation into
265 more crystalline and refractory minerals. This interaction is evidenced experimentally (53), and
266 by observations that show that one fifth of marine sedimentary OC is bound to reactive Fe
267 phases (54), which are predominantly nano-scale oxyhydroxides in marine sediment oxic layers
268 (47). Therefore, Lalonde *et al.*'s (54) proposition of a “rusty sink”, in which formation of meta-
269 stable Fe(III) organo-minerals promotes OC burial, may here prove to be a “rusty source”
270 mechanism for the occurrence of cFe in oxic porewater. In other words, our assessment of core-
271 top TOC and cFe content could reflect the availability of OC compounds formed during organic
272 matter degradation and that are suited to stabilisation of nano-scale Fe oxyhydroxide.

273

274 **Mechanisms governing the production of porewater Fe solutes and mineral colloids.** It
275 is important to determine whether cFe in oxidising porewater is an authigenic precipitate of Fe
276 produced by RD or if it has formed by a distinctly non-reductive pathway, because these
277 processes of colloid production (or within our operational definitions here, sediment-
278 dissolution) will have different drivers and impacts in the ocean and may respond and feed back
279 differently to changes in the overlying ocean environment. Addressing this issue is essential if
280 we are to build confidence in the paradigms we depend upon to estimate the size and variability
281 of iron inputs in ocean biogeochemical models (3, 4, 18).

282

We can simulate the steady-state porewater production/consumption profiles needed to
283 reproduce measured soluble, dissolved, and colloidal Fe concentration profiles across an oxic-

284 nitrogenous zone. Of the GA10W transect, Station 21 offers uniquely detailed data resolution
285 to perform this assessment with the 1-dimensional steady-state “Rate Estimates from
286 Concentration profiles” or REC model previously described by Lettman *et al.* (55). If we
287 impose a lower boundary condition for sFe and dFe concentrations equal to porewater values
288 at 9.5 cmbsf, and a surface boundary condition of 1 nmol L⁻¹ to approximate bottom water (24),
289 model fits to sFe and dFe data (and cFe by difference) may be calculated (Fig. 4).

290 The sFe profile is reproduced with a single region of production in the ferruginous zone
291 (>7.5 cmbsf) and a single region of consumption above it (5-7.5 cmbsf) in accordance with the
292 oxidising potential of nitrous oxides. A more complex production profile is required to simulate
293 dFe, which is predominantly determined by the production of cFe rather than sFe. Production
294 of cFe coincides with a region of sFe consumption (between 5 and 7.5 cmbsf), indicating sFe-
295 oxidation could partially contribute an authigenic source to cFe in porewater. However, the dFe
296 profile requires similar magnitudes of cFe production in oxic, nitrogenous, and ferruginous
297 zones. Therefore, sFe oxidation alone does not fully account for the production of cFe.

298

299 **Porewater isotopic constraints on the genesis of colloidal Fe.** We can further test
300 hypothetical controls on the genesis of cFe using an isotopic mass-balance model. We consider
301 two scenarios in which the isotopic composition of dFe is determined by theoretical controls
302 on soluble and colloidal Fe species: In the first scenario, sFe (assumed here to be Fe(II)_{aq}) is
303 oxidised and isotopically fractionated, and cFe is assumed to form entirely from the authigenic
304 products of sFe oxidation. In the second scenario, sFe is oxidised and isotopically fractionated,
305 but removed to the sediment, and cFe is formed entirely from the oxidative weathering of
306 lithogenic material without any Fe isotope fractionation. Initial isotope ratios for sFe and cFe
307 can be adjusted so that the resultant dFe isotope ratio matches the observed value at the dFe
308 maxima 9.5 cmbsf. The isotope compositions of sFe and authigenic cFe can then be determined
309 by an isotope fractionation factor (α) during Fe(II)_{aq} oxidation. Herein we choose to evaluate
310 values of $\alpha < 1$ and > 1 , such that $\Delta_{\text{sFe-cFe}}$ was $\pm 0.5\%$ (SI Appendix, SI Text 2).

311 By modelling these idealised controls on the isotopic composition of porewater dFe,
312 we make two interesting observations. Firstly, porewater dFe isotopes cannot be reproduced
313 when oxidation of sFe determines the isotope composition of cFe (Figure 5ab), whereas dFe
314 isotopes are reproduced quite well when cFe reflects a homogenous crustal weathering product
315 (Figure 5cd). Secondly, dFe isotopes are most accurately reproduced at the transition between
316 ferruginous and oxic-nitrogenous conditions (i.e. region of maximum sFe consumption; *c.f.* Fig.
317 4) when α is < 1 . We achieve our best simulation of porewater dFe isotopes when cFe is
318 lithogenic and sFe is consumed by oxidation with α of 0.9995 (Figure 5d).

319 We note that the nature of authigenic mineral sinks linked to sFe oxidation will be more
320 complex than has been represented in our simplified approach to isotopic mass-balance above.
321 For example, sFe oxidation may be catalysed by NO₃-reducing Fe(II)-oxidizing bacteria - most
322 prevalent in marine sediments with low to moderate TOC content (56). Siderite (Fe(II)CO₃) is
323 also a common authigenic precipitate of Fe(II)_{aq} that produces kinetic and equilibrium isotope
324 effects (Fe(II)_{aq}-FeCO₃ = $\Delta + 1.2$ and 0.0% , respectively (57)).

325 Crucially, however, authigenic Fe minerals must either preserve or fractionate isotope
326 ratios from their source of aqueous Fe(II). If Fe(II) is produced from ferruginous depths in
327 porewater following conventional RD theory then any such authigenic minerals must either
328 preserve (e.g. *via* siderite) or fractionate (e.g. *via* oxidation to ferrihydrite) the light isotope
329 composition of the Fe(II) supplied from the ferruginous zone. Because we have chosen to
330 consider a range of α values (from 0.9995 to 1.0005), our simulations may represent a wide

331 range of potential isotope fractionations that might reasonably be achieved by formation of
332 common authigenic Fe minerals (40, 41, 57, 58) or by complexation of soluble Fe with organic
333 ligands (26, 50). Yet we still determine colloidal Fe isotopes to be almost uniformly identical
334 to the continental crust, within and between ocean basins. This occurs in the presence of
335 contrasting sediment composition (e.g. opaline, carbonate, basaltic, siliciclastic and TOC
336 content) between sites. Such compositional variability would theoretically encourage variations
337 in the solubility of different authigenic phases, and therefore impart different isotope
338 fractionation effects upon $\text{Fe(II)}_{\text{aq}}$ between sites, but this variability in the cFe pool is simply
339 not observed (Fig. 3). For these reasons we consider that cFe is principally formed by oxidative
340 weathering of lithogenic material without dissimilatory reduction and isotope fractionation by
341 bacteria. While bacterial siderophores may promote Fe oxide and Fe-bearing silicate mineral
342 dissolution, they can do so indirectly via proton-promoted dissolution (59), which does not
343 fractionate Fe isotopes (60). We posit that nano-scale ferrihydrite produced by oxidative
344 weathering is further stabilised by the sorption of OC, but sorption to the Fe mineral surface
345 imparts no fractionation effect and therefore preserves its Fe isotope composition.

346

347 **Implications for the ocean Fe inventory.** A lithological source of Fe colloids in surface
348 oxidising porewater has important implications for our assessment of benthic Fe supply to the
349 ocean. The oxidising conditions reported here reflect those that occur commonly below the
350 sediment-water interface of major open ocean margins and basins (36). Thus we provide key
351 new evidence to further disqualify the assumption that only RD controls benthic input of
352 dissolved iron to the ocean (8, 9). Organo-mineral Fe weathering products with a longer oceanic
353 residence time than reduced Fe species may explain how dFe bearing non-reductive crustal
354 isotopic signatures can escape the seafloor and be transported to the ocean interior.

355 The resultant flux of lithogenic Fe colloids to the ocean will reflect the balance of *in*
356 *situ* production rates and benthic exchange mechanisms (Fig. 6). We find that the absolute
357 abundance of cFe in porewater remains greatest in sediments composed of fresh basaltic
358 weathering products, likely indicative of the higher Fe and Mn contents of mafic source rocks
359 and the susceptibility of mafic minerals (e.g. basalt glass, olivine, amphibole) to weather rapidly
360 and produce Fe(oxy)hydroxides and clays during marine early diagenesis (*c.f.* Fig. 2b). We also
361 find that OC is an important additional factor in the production of cFe, but we can only speculate
362 as to the nature of OC moieties in porewater that might elicit the strong cFe relationship with
363 TOC observed in South Atlantic sediments. We suggest that degradation of organic matter may
364 yield bacterial communities and compounds with functional groups suited to (a) enhance the
365 oxidative weathering Fe oxide and Fe-bearing silicate minerals (59), and (b) the sorption of
366 Fe(oxy)hydroxides present in oxic zones (61), which inhibits the loss of Fe to more crystalline
367 phases and encourages preservation as nano-minerals (54). If so, then seafloor organic carbon
368 supply may still exert an important overarching influence on sedimentary dFe fluxes to the
369 ocean, only here it is due to enhanced non-reductive dissolution and mineral-protection effects,
370 rather than reductive dissolution or ionic complexation processes that fractionate Fe isotopes
371 (5, 26).

372 Benthic exchange mechanisms will promote the flux of cFe produced by seafloor
373 weathering and OC complexation to the ocean interior (Fig. 6). Established gradients in cFe
374 concentration between porewater and bottom water may promote a diffusive flux of colloids
375 towards the deep ocean. Without knowledge of cFe diffusion coefficients, diffusive flux
376 calculations may inaccurately need to assume their behaviours match those of the aqueous ion.
377 On the other hand, the stability of organo-mineral colloids in the presence of oxygen means

378 that large reactive losses, such as those required to account for oxidation of aqueous Fe(II) (7,
379 12), may not be applicable to an assessment of cFe (28). Of further significance, biophysical
380 activity and bottom shear stress will promote the entrainment of surface sediment and
381 porewaters in the ocean (46, 62). These entrainments can encourage the scavenging-removal of
382 aqueous Fe(II) and Fe(III) species present in excess of ligand concentrations (e.g. (12)), and
383 simultaneously promote the exchange of mineral solids (including colloids) between the
384 sediments and the water column (27, 29). Energy for the generation and transport of a benthic
385 nepheloid inventory appears unevenly in the ocean. It is tied to upper ocean dynamics and the
386 internal tide and is compounded by bathymetric roughness, island mass effects and reflection
387 angles (29, 63, 64). Despite complexity to these interactions, their importance for boundary
388 exchange and transport in the ocean is well recognised (16, 30) and even evidenced to facilitate
389 the supply of cFe (23, 27) and lithogenic Fe isotopes to the water column (20) (Fig. 6).

390 Where sites of maximum cFe production and potential benthic entrainment overlap,
391 conditions suited to produce a flux of cFe and crustal isotope signatures to the ocean ought to
392 be optimised (Fig. 7). Improved knowledge of where cFe fluxes occur would assist their
393 inclusion in new generations of ocean iron cycle models, which would, in turn, provide an
394 opportunity to update our understanding of how sedimentary iron supply impacts the ocean
395 carbon cycle (2). Optimal conditions for sedimentary cFe input in the ocean may be predicted,
396 firstly, by considering the known surface exchangeable (0-1 cmbsf) inventory of porewater Fe
397 bearing crustal isotope compositions (Fig. 7a). Large differences exist in the dFe isotopic
398 signature of surface exchangeable porewater in the upper 1500m of the ocean with a tendency
399 towards light values that are attributable to the variable influence of reductive and non-
400 reductive sediment dissolution. By contrast the isotopic signatures from equivalent porewater
401 depths are far more uniform and crustal in ocean sediments beneath 1500m due to the lithogenic
402 production of cFe in oxic-nitrogenous zones. These sites also correspond to low benthic oxygen
403 consumption rates ($<2 \text{ mmol m}^{-2} \text{ d}^{-1}$) sufficient to suppress the generation of sFe by RD in
404 ferruginous zones well below the sediment-water interface. Secondly, the entrainment potential
405 for cFe is illustrated by comparing compilations of benthic O_2 flux (sediment community O_2
406 consumption rates (65)) and the benthic nepheloid inventories observed in bottom water (29)
407 (Fig. 7b). Sediments below 1500m water depth exhibit the lowest rates of O_2 consumption,
408 almost exclusively $<2 \text{ mmol m}^{-2} \text{ d}^{-1}$, so that they are most likely to contain exchangeable
409 porewater inventories of lithogenic cFe (*c.f.* Fig. 7a). Bottom waters bearing the highest benthic
410 nepheloid inventories are also found in deep waters, notably in western margins and basins of
411 the North and South Atlantic Ocean, indicating that these regions could optimise the
412 entrainment of cFe and lithogenic isotopes in the ocean. Shelf and slope sediments above
413 1500m, show the highest benthic fluxes of O_2 , consistent with these regions supporting
414 reservoirs of reduced, soluble and light Fe isotopes in porewaters that can be exchanged with
415 the upper ocean (7, 11). A high degree of variation to benthic nepheloid inventories and oxygen
416 flux (<1 to $>10 \text{ mmol m}^{-2} \text{ d}^{-1}$) is also shown in sediments above 1500m (Fig. 7b) and suggests
417 the relative contributions of RD and NRD might vary considerably between regions of the upper
418 ocean.

419 Further localised and seasonal variations in sediment dissolution and mechanisms of
420 entrainment are certain to exist, particularly close to margins, that are not represented by the
421 data or grid resolution presented here. The exchangeable inventories of cFe in oxidising
422 porewaters will also respond to the underlying influence of igneous provenance and OC (*c.f.*
423 Fig. 2b), which we have not explicitly accounted for. Therefore, the broader implications of our
424 findings are potentially significant but not yet known. The stability of organo-mineral Fe

425 colloids means they may not succumb to the same fate (rapid precipitation, aggregation, and
426 removal) that limits the extent to which reductive Fe inputs influence the ocean interior. By the
427 same token, the bioavailability of these organo-mineral Fe colloids is unknown, and begs the
428 question: Is there a trade-off between the endurance of Fe colloids in the ocean and their
429 accessibility for phytoplankton? An additional, more stable source of dFe deeper in the water
430 column governed by lithogenic colloid production, which has been ignored in our earlier
431 numerical and conceptual models of the iron cycle, will contribute to the buffering of the ocean
432 dFe inventory against variability from other sources and lower further the mean residence time
433 of dFe.

434

435 **Conclusions**

436 South Atlantic Sediments contain a non-linear down slope gradient in O₂ consumption rates,
437 with coupled porewater depth zonation of nitrous oxide, Mn oxide, and Fe oxide reduction
438 pathways, which are consistent with anticipated down-slope gradients in OC flux and
439 decomposition at the ocean floor. Porewater maxima in dissolved Fe contents have light Fe
440 isotopic composition in the form of mostly soluble Fe species, reflecting the reductive-
441 dissolution of Fe(III) to Fe(II) by bacteria in ferruginous zones. Beneath these maxima in
442 dissolved Fe contents, heavy dissolved Fe isotopes corresponded to the reactive loss of soluble
443 Fe(II) with free sulphide. Detectable amounts of dissolved Fe in the overlying oxic-nitrogenous
444 zones have dissolved Fe isotope compositions that are indistinguishable from average igneous
445 weathering products due to the production of Fe colloids from lithogenic weathering. Based on
446 a strong correlation between colloidal Fe abundance and TOC, we propose colloidal Fe stability
447 may be promoted by Fe(oxyhydr)oxide adsorption to OC and the formation of nano-scale
448 ferrihydrite organo-mineral composites.

449 Modelled porewater production and consumption profiles indicate that a soluble Fe
450 pool of Fe(II) accounts for the light isotopic composition of ferruginous zones, whereas
451 dissolved Fe and its isotope composition was mostly determined by the genesis of colloidal Fe
452 in overlying oxic-nitrogenous zones of marine sediments. Our isotopically-constrained model
453 experiments show that non-reductive weathering of lithogenic material is required to account
454 for the widespread occurrence of colloidal Fe in porewater – oxidative conversion of soluble
455 Fe(II) to colloidal Fe(III) alone, was an insufficient explanation for the presence of Fe colloids
456 and their isotope composition, as were alternative authigenic mineral or ligand-stabilised
457 “sinks” for soluble Fe(II) supplied by reductive dissolution.

458 We determine that oxic-nitrogenous ocean sediments are sites of lithogenic weathering
459 and organo-mineral formation that will be provide a “rusty source” of colloidal Fe throughout
460 the global ocean. Coupled to the generation of benthic nepheloid inventories, oxidising
461 sediments will be important sites for benthic Fe exchange that need to be reappraised for their
462 role in ocean biogeochemical cycles.

463

464

465 **Materials and methods**

466

467 A Bowers Connelly Mega Corer collected multiple intact surface sediment cores from 6 sites
468 in the South Atlantic during occupation by the RRS *James Cook* (JC068) in 2011. All cores
469 were transferred to a controlled temperature laboratory replicating bottom water conditions
470 (4-8°C) for microsensor profiling and porewater extraction, where all apparatus in contact
471 with the samples (syringes, Teflon, centrifuge tubes and Low-Density Polyethylene (LDPE)

472 bottles were cleaned prior to use (72 hours in 10% Decon; 72 hours in 6M HCl; 72 hours in
473 6M HNO₃; rinsed by 18.2MΩ deionised water).

474 Microsensor determinations of dissolved oxygen were performed by a Unisense micro-
475 profiling suite of apparatus following analytical procedures previously described and used in
476 coastal and deep-sea sediments elsewhere (7, 9, 28). Oxygen penetration depths were either
477 measured directly in the upper 6cm or estimated from model fits to steady state oxygen
478 consumption rates as previously described (7, 9).

479 Rhizon samplers (2.5 x 50 mm “CSS” type, Rhizosphere Research Products) were
480 inserted at 1cm depth intervals through pre-drilled holes into a second sediment core recovered
481 from the Mega Core deployment. Porewater was filtered (~0.15 μm) by suction through each
482 Rhizon into a BD Discardit syringe in an ambient atmosphere. Sample aliquots (2 ml) were
483 diluted 15-fold by 18.2 MΩ deionised water and stored in the dark prior to ship-board nutrient
484 analyses (NO₃⁻, NO₂⁻, NH₄⁺) by a 5-channel Bran and Luebbe AAIII segmented flow
485 colorimetric auto analyser after Homoky *et al.* (9) and previously reported by Bridgestock *et*
486 *al.* (66).

487 Under a nitrogen atmosphere, a third sediment core was extruded, sliced at 1cm depth
488 intervals, and centrifuged at 9,000g for 6 minutes, before supernatant porewaters were siphoned
489 through Teflon tubes into BD Discardit syringes. Samples for dissolved metals were passed
490 through Whatmann Puradisc 25 syringe filters with polyethersulphone membranes (0.2 μm)
491 and selected sub-samples for soluble metals were passed through a second, in-line Whatman
492 Anatop 25 syringe filter with aluminium oxide membrane (0.02 μm). All porewater samples
493 were later acidified to pH<2 by adding 6 μl of 6M quartz distilled (Q) HCl per millilitre of
494 sample and stored refrigerated prior to analyses.

495 Sediment residues from centrifugation were freeze dried under vacuum and later
496 pulverised in an agate pestle and mortar for carbon, and opal determinations. The bulk
497 composition of sediment cores is described by dry-mass measurements of the total carbonate
498 (CaCO₃), total organic carbon (TOC), opal and - by difference from the total dry mass -
499 lithogenic material. The difference between coulometric determination (UIC 5012 Coulometer)
500 of total carbon (TC) and total inorganic carbon (TIC) content of powdered sediments were used
501 to calculate TOC. TC was calculated from CO₂ released during sample combustion, and TIC
502 was calculated from CO₂ released during heated sample reaction with 1.5 M H₃PO₄. Accuracy
503 of TC and TIC determinations was assessed with anhydrous CaCO₃ powder, with a mean
504 recovery of 100.4±0.8% (1SD, n=15). The limit of detection (LOD = 3SD of blanks) was 10
505 mg C, equivalent to 0.03 wt% TOC. Opal content was measured by molybdate blue
506 spectrometry on Si extracted solutions from dry homogenized sediments following the sodium
507 bicarbonate sequential leaching method according to Mortlock and Froelich (67). Accuracy of
508 opal determination was assessed by multiple analyses of a laboratory bulk sediment at the
509 School of Geosciences, University of Edinburgh with a reproducibility of 1.54%.

510 A Thermo Scientific Element X2 Inductively Coupled Plasma-Mass Spectrometer
511 (ICP-MS) was used to determine the concentration of aqueous metals in acidified porewater
512 samples and sediment digests following Homoky *et al.* (9) and previously reported by
513 Bridgestock *et al.* (66). Briefly, porewaters were diluted 100-fold with 0.48 M Q-HNO₃, and
514 external calibration standards were matrix matched to samples with 1% of the seawater
515 standard NASS-5 (National Research Council Canada). The mass of ⁴⁵Sc spiked to all
516 samples was used as an internal standard to monitor and correct for a reduction in signal
517 intensity of over time. Accuracy of the method was verified by the intermittent analysis of
518 blank-bracketed SLRS-5 (National Research Council Canada) within certified values, with a

519 RSD of 1.1 and 1.3% for Fe and Mn respectively. The LOD (3SD of analytical blanks, $n=9$)
520 for reported Fe and Mn were 1 and 0.1 nmol l⁻¹, and procedural blanks were below these
521 limits of detection.

522 Dissolved Fe isotopic compositions from porewaters were measured following
523 previously published methods (9, 68). Aliquots of porewater containing Fe inventories from 20
524 to 104 ng were spiked with an ⁵⁷Fe-⁵⁸Fe double spike (in a 1:2 sample:spike ratio), evaporated
525 to dryness in 7 mL Savillex™ PFA Teflon vials, and then re-dissolved in 5 M quartz-distilled
526 HCl + 0.001% v/v Optima H₂O₂ before being passed through 135 µL AGMP-1 column
527 purification. Fe was eluted from the columns in 0.8 mL of 1M quartz-distilled HCl and
528 evaporated to dryness before being re-dissolved in 0.5 mL of 0.1 M Teflon-distilled HNO₃ for
529 analysis by Multi Collector (MC)-ICPMS. Procedural blanks for this method have previously
530 been shown to be 3 ng of Fe per sample (9). Samples were then analysed for Fe isotopic
531 composition by Thermo Neptune MC-ICPMS with jet interface at the University of South
532 Carolina, using an ESI Apex-Q introduction system, Pt Jet and Al X cones, following methods
533 identical to those described previously (9). Fe isotopic compositions ($\delta^{56}\text{Fe}$) are expressed in
534 typical delta notation relative to the IRMM-014 international Fe standard. The accuracy of this
535 procedure has been previously demonstrated on seawater samples (68, 69), and here we assign
536 0.05‰ as an estimate of external precision of analysis, based on duplicate measurements of 60
537 GA10 seawater samples (0.1-1.8 nmol kg⁻¹), measured over multiple analytical sessions during
538 the same time interval (69). In cases where the 2 standard internal error is larger than 0.05‰,
539 we consider the 2SE a more representative estimate of uncertainty.

540

541 Acknowledgments

542 We thank the captain and crew of the *RRS James Cook* expedition JC068, and science party
543 of UK-GEOTRACES GA10W. In particular Deborah Hembury and Yu-Te Hsieh (University
544 of Oxford) for shipboard sampling assistance, Malcolm Woodward (Plymouth Marine
545 Laboratory) for shipboard nutrient analyses, and Alex Thomas (University of Edinburgh) for
546 supporting opal analyses by FD. RAM supported WBH for the collection of sediments and
547 porewater and analyses of oxygen, metals and carbon through NERC grants
548 (NE/F017197/1 and NE/H004394/1). WBH was independently supported by
549 a NERC fellowship at University of Oxford (NE/K009532/1) to prepare samples for Fe
550 isotope analyses and perform model experiments, and by a University Academic Fellowship
551 at University of Leeds to write the manuscript. Fe isotope analyses by TMC and SGJ were
552 supported by the University of South Carolina. DK and AT were funded by European
553 Research Council under the European Union's Horizon 2020 research and innovation
554 program (grant agreement 724289).

555

556 References

557

- 558 1. V. A. Elrod, W. M. Berelson, K. H. Coale, K. S. Johnson, The flux of iron from
559 continental shelf sediments: a missing source for global budgets. *Geophys Res Lett*
560 **31**, L12307 (2004).
- 561 2. A. Tagliabue, O. Aumont, L. Bopp, The impact of different external sources of iron
562 on the global carbon cycle. *Geophysical Research Letters* **41**, 920-926 (2014).
- 563 3. W. B. Homoky *et al.*, Quantifying trace element and isotope fluxes at the ocean-
564 sediment boundary: a review. *Philosophical Transactions of the Royal Society A:*
565 *Mathematical, Physical and Engineering Sciences* **374** (2016).
- 566 4. A. Tagliabue *et al.*, How well do global ocean biogeochemistry models simulate
567 dissolved iron distributions? *Global Biogeochemical Cycles* **30**, 149-174 (2016).

- 568 5. S. Severmann, C. M. Johnson, B. L. Beard, J. McManus, The effect of early
569 diagenesis on the Fe isotope compositions of porewaters and authigenic minerals in
570 continental margin sediments. *Geochimica et Cosmochimica Acta* **70**, 2006-2022
571 (2006).
- 572 6. W. B. Homoky, S. Severmann, R. A. Mills, P. J. Statham, G. R. Fones, Pore-fluid Fe
573 isotopes reflect the extent of benthic Fe redox recycling: Evidence from continental
574 shelf and deep-sea sediments. *Geology* **37**, 751-754 (2009).
- 575 7. J. K. Klar *et al.*, Stability of dissolved and soluble Fe(II) in shelf sediment pore
576 waters and release to an oxic water column. *Biogeochemistry* 10.1007/s10533-017-
577 0309-x, 1-19 (2017).
- 578 8. A. Radic, F. Lacan, J. W. Murry, Iron isotopes in the seawater of the equatorial
579 Pacific Ocean: New constraints for the oceanic iron cycle. *Earth and Planet. Sci. Lett.*
580 **306**, 1-10 (2011).
- 581 9. W. B. Homoky, S. G. John, T. Conway, R. A. Mills, Distinct iron isotopic signatures
582 and supply from marine sediment dissolution. *Nature Communications* **4** (2013).
- 583 10. I. Rapp *et al.*, El Niño-Driven Oxygenation Impacts Peruvian Shelf Iron Supply to the
584 South Pacific Ocean. *Geophysical Research Letters* **47**, e2019GL086631 (2020).
- 585 11. S. Severmann, J. McManus, W. M. Berelson, D. E. Hammond, The continental shelf
586 benthic iron flux and its isotope composition. *Geochimica et Cosmochimica Acta* **74**,
587 3984-4004 (2010).
- 588 12. W. B. Homoky *et al.*, Dissolved oxygen and suspended particles regulate the benthic
589 flux of iron from continental margins. *Marine Chemistry* **134-135**, 59-70 (2012).
- 590 13. S. G. John, J. Mendez, J. Moffett, J. Adkins, The flux of iron and iron isotopes from
591 San Pedro Basin sediments. *Geochimica et Cosmochimica Acta* **93**, 14-29 (2012).
- 592 14. A. Noffke *et al.*, Benthic iron and phosphorous fluxes across the Peruvian oxygen
593 minimum zone. *Limnol. Oceanogr.* **57**, 851-867 (2012).
- 594 15. M. Staubwasser, R. Schoenberg, F. von Blanckenburg, S. Krüger, C. Pohl, Isotope
595 fractionation between dissolved and suspended particulate Fe in the oxic and anoxic
596 water column of the Baltic Sea. *Biogeosciences* **10**, 233-245 (2013).
- 597 16. P. J. Lam, M. I. Heller, P. E. Lerner, J. W. Moffett, K. N. Buck, Unexpected Source
598 and Transport of Iron from the Deep Peru Margin. *ACS Earth and Space Chemistry* **4**,
599 977-992 (2020).
- 600 17. F. Scholz, S. Severmann, J. McManus, C. Hensen, Beyond the Black Sea paradigm:
601 The sedimentary fingerprint of an open-marine iron shuttle. *Geochimica et*
602 *Cosmochimica Acta* **127**, 368-380 (2014).
- 603 18. A. W. Dale *et al.*, A revised global estimate of dissolved iron fluxes from marine
604 sediments. *Global Biogeochemical Cycles* **29**, 691-707 (2015).
- 605 19. J. J. Middelburg, K. Soetaert, P. M. J. Herman, Empirical relationships for use in
606 global diagenetic models. *Deep Sea Research Part I: Oceanographic Research*
607 *Papers* **44**, 327-344 (1997).
- 608 20. T. M. Conway, S. G. John, Quantification of dissolved iron sources to the North
609 Atlantic Ocean. *Nature* **511**, 212-215 (2014).
- 610 21. M. Labatut *et al.*, Iron sources and dissolved-particulate interactions in the seawater
611 of the Western Equatorial Pacific, iron isotope perspectives. *Global Biogeochemical*
612 *Cycles* **28**, 1044-1065 (2014).
- 613 22. C. Abadie, F. Lacan, A. Radic, C. Pradoux, F. Poitrasson, Iron isotopes reveal distinct
614 dissolved iron sources and pathways in the intermediate versus deep Southern Ocean.
615 *Proceedings of the National Academy of Sciences* **114**, 858-863 (2017).
- 616 23. J. N. Fitzsimmons *et al.*, Partitioning of dissolved iron and iron isotopes into soluble
617 and colloidal phases along the GA03 GEOTRACES North Atlantic Transect. *Deep*
618 *Sea Research Part II: Topical Studies in Oceanography* **116**, 130-151 (2015).
- 619 24. R. Schlitzer *et al.*, The GEOTRACES Intermediate Data Product 2017. *Chemical*
620 *Geology* **493**, 210-223 (2018).

- 621 25. K. Kuma, A. Katsumoto, J. Nishioka, K. Matsunaga, Size-fractionated iron
622 concentrations and Fe(III) hydroxide solubilities in various coastal waters. *Estuarine,*
623 *Coastal and Shelf Science* **47**, 275-283 (1998).
- 624 26. K. Dideriksen, J. A. Baker, S. L. S. Stipp, Fe isotope fractionation between inorganic
625 aqueous Fe(III) and a Fe siderophore complex. *Mineral Mag* **72**, 313-316 (2008).
- 626 27. K. Kunde *et al.*, Iron Distribution in the Subtropical North Atlantic: The Pivotal Role
627 of Colloidal Iron. *Global Biogeochemical Cycles* **n/a**.
- 628 28. W. B. Homoky *et al.*, Iron and Manganese diagenesis in deep sea volcanogenic
629 sediments and the origins of pore water colloids. *Geochim. Cosmochim. Acta* **75**,
630 5032-5048 (2011).
- 631 29. W. D. Gardner, M. J. Richardson, A. V. Mishonov, Global assessment of benthic
632 nepheloid layers and linkage with upper ocean dynamics. *Earth and Planetary*
633 *Science Letters* **482**, 126-134 (2018).
- 634 30. J. C. Latimer, G. M. Filippelli, Sedimentary iron records from the Cape Basin. *Deep*
635 *Sea Research Part II: Topical Studies in Oceanography* **54**, 2422-2431 (2007).
- 636 31. W. Weijer, M. E. Maltrud, W. B. Homoky, K. L. Polzin, L. R. M. Maas, Eddy-driven
637 sediment transport in the Argentine Basin: Is the height of the Zapiola Rise
638 hydrodynamically controlled? *Journal of Geophysical Research: Oceans* **120**, 2096-
639 2111 (2015).
- 640 32. R. C. Thunell, Carbonate dissolution and abyssal hydrography in the Atlantic Ocean.
641 *Marine Geology* **47**, 165-180 (1982).
- 642 33. T. J. Shaw, J. M. Gieskes, R. A. Jahnke, Early diagenesis in differing depositional
643 environments: The response of transition metals in pore water. *Geochimica et*
644 *Cosmochimica Acta* **54**, 1233-1246 (1990).
- 645 34. B. L. Beard *et al.*, Application of Fe isotopes to tracing the geochemical and
646 biological cycling of Fe. *Chemical Geology* **195**, 87-117 (2003).
- 647 35. A. Dutkiewicz, R. D. Müller, S. O'Callaghan, H. Jónasson, Census of seafloor
648 sediments in the world's ocean. *Geology* 10.1130/g36883.1 (2015).
- 649 36. R. N. Glud, Oxygen dynamics of marine sediments. *Marine Biology Research* **4**, 243-
650 289 (2008).
- 651 37. P. N. Froelich *et al.*, Early oxidation of organic matter in pelagic sediments of the
652 eastern equatorial Atlantic: suboxic diagenesis. *Geochimica et Cosmochimica Acta*
653 **43**, 1075-1090 (1979).
- 654 38. S. Henkel, S. Kasten, J. F. Hartmann, A. Silva-Busso, M. Staubwasser, Iron cycling
655 and stable Fe isotope fractionation in Antarctic shelf sediments, King George Island.
656 *Geochimica et Cosmochimica Acta* **237**, 320-338 (2018).
- 657 39. S. Henkel, S. Kasten, S. W. Poulton, M. Staubwasser, Determination of the stable
658 iron isotopic composition of sequentially leached iron phases in marine sediments.
659 *Chemical Geology* **421**, 93-102 (2016).
- 660 40. L. Wu, B. L. Beard, E. E. Roden, C. M. Johnson, Stable Iron Isotope Fractionation
661 Between Aqueous Fe(II) and Hydrous Ferric Oxide. *Environmental Science &*
662 *Technology* **45**, 1847-1852 (2013).
- 663 41. B. L. Beard *et al.*, Iron isotope fractionation between aqueous ferrous iron and
664 goethite. *Earth and Planetary Science Letters* **295**, 241-250 (2010).
- 665 42. A. J. Birchill *et al.*, Seasonal iron depletion in temperate shelf seas. *Geophysical*
666 *Research Letters* **44**, 8987-8996 (2017).
- 667 43. M. Gledhill, K. N. Buck, The organic complexation of iron in the marine
668 environment: a review. *Frontiers in Microbiology* **3**, 1-17 (2012).
- 669 44. P. H. Santschi, Marine colloids, agents of the self-cleansing capacity of aquatic
670 systems: Historical perspective and new discoveries. *Marine Chemistry* **207**, 124-135
671 (2018).
- 672 45. M. L. Wells, E. D. Goldberg, Marine submicron particles. *Marine Chemistry* **40**, 5-18
673 (1992).

- 674 46. R. Raiswell, D. E. Canfield, The Iron Biogeochemical Cycle Past and Present.
675 *Geochemical Perspectives* **1**, 1-2 (2012).
- 676 47. C. van der Zee, D. R. Roberts, D. G. Rancourt, C. P. Slomp, Nanogoethite is the
677 dominant reactive oxyhydroxide phase in lake and marine sediments. *Geology* **31**,
678 993-996 (2003).
- 679 48. A. Gartman, A. J. Findlay, G. W. Luther, Nanoparticulate pyrite and other
680 nanoparticles are a widespread component of hydrothermal vent black smoker
681 emissions. *Chemical Geology* **366**, 32-41 (2014).
- 682 49. A. D. Anbar, O. Rouxel, Metal Stable Isotopes in Paleooceanography. *Annual Review*
683 *of Earth and Planetary Sciences* **35**, 717-746 (2007).
- 684 50. E. Lotfi-Kalahroodi *et al.*, Iron isotope fractionation in iron-organic matter
685 associations: Experimental evidence using filtration and ultrafiltration. *Geochimica et*
686 *Cosmochimica Acta* **250**, 98-116 (2019).
- 687 51. M. T. Jones *et al.*, Quantifying the impact of riverine particulate dissolution in
688 seawater on ocean chemistry. *Earth and Planetary Science Letters* **395**, 91-100
689 (2014).
- 690 52. C. Jeandel, Overview of the mechanisms that could explain the ‘Boundary Exchange’
691 at the land–ocean contact. *Philosophical Transactions of the Royal Society A:*
692 *Mathematical, Physical and Engineering Sciences* **374**, 20150287 (2016).
- 693 53. L. K. ThomasArrigo, J. M. Byrne, A. Kappler, R. Kretzschmar, Impact of Organic
694 Matter on Iron(II)-Catalyzed Mineral Transformations in Ferrihydrite–Organic Matter
695 Coprecipitates. *Environmental Science & Technology* **52**, 12316-12326 (2018).
- 696 54. K. Lalonde, A. Mucci, A. Ouellet, Y. G elinas, Preservation of organic matter in
697 sediments promoted by iron. *Nature* **483**, 198-200 (2012).
- 698 55. K. A. Lettmann *et al.*, Estimation of biogeochemical rates from concentration
699 profiles: A novel inverse method. *Estuarine, Coastal and Shelf Science* **100**, 26-37
700 (2012).
- 701 56. K. Laufer, H. R oy, B. B. J orgensen, A. Kappler, Evidence for the Existence of
702 Autotrophic Nitrate-Reducing Fe(II)-Oxidizing Bacteria in Marine Coastal Sediment.
703 *Applied and Environmental Microbiology* **82**, 6120 (2016).
- 704 57. C. M. Johnson, E. E. Roden, S. A. Welch, B. L. Beard, Experimental constraints on
705 Fe isotope fractionation during magnetite and Fe carbonate formation coupled to
706 dissimilatory hydrous ferric oxide reduction. *Geochimica et Cosmochimica Acta* **69**,
707 963 (2005).
- 708 58. L. Wu, G. Druschel, A. Findlay, B. L. Beard, C. M. Johnson, Experimental
709 determination of iron isotope fractionations among $\text{Fe}^{2+}(\text{aq})$ - $\text{FeS}(\text{aq})$ -Mackinawite
710 at low temperatures: Implications for the rock record. *Geochimica et Cosmochimica*
711 *Acta* **89**, 46-61 (2012).
- 712 59. S. M. Kraemer, Iron oxide dissolution and solubility in the presence of siderophores.
713 *Aquatic Sciences* **66**, 3-18 (2004).
- 714 60. J. G. Wiederhold *et al.*, Iron Isotope Fractionation during Proton-Promoted, Ligand-
715 Controlled, and Reductive Dissolution of Goethite. *Environmental Science &*
716 *Technology* **40**, 3787-3793 (2006).
- 717 61. C. B. Kennedy, S. D. Scott, F. G. Ferris, Hydrothermal phase stabilization of 2-line
718 ferrihydrite by bacteria. *Chemical Geology* **212**, 269-277 (2004).
- 719 62. F. Couceiro *et al.*, Impact of resuspension of cohesive sediments at the Oyster
720 Grounds (North Sea) on nutrient exchange across the sediment–water interface.
721 *Biogeochemistry* **113**, 37-52 (2013).
- 722 63. D. A. Cacchione, W. D. Grant, D. E. Drake, S. M. Glenn, Storm-Dominated Bottom
723 Boundary Layer Dynamics on the Northern California Continental Shelf:
724 Measurements and Predictions. *Journal of Geophysical Research* **92**, 1817-1827
725 (1987).
- 726 64. D. A. Cacchione, L. F. Pratson, A. S. Ogston, The Shaping of Continental Slopes by
727 Internal Tides. *Science* **296**, 724 (2002).

- 728 65. T. Stratmann, K. Soetaert, C.-L. Wei, Y.-S. Lin, D. van Oevelen, The SCOC
 729 database, a large, open, and global database with sediment community oxygen
 730 consumption rates. *Scientific Data* **6**, 242 (2019).
 731 66. L. Bridgestock *et al.*, Controls on the barium isotope compositions of marine
 732 sediments. *Earth and Planetary Science Letters* **481**, 101-110 (2018).
 733 67. R. A. Mortlock, P. N. Froelich, A simple method for the rapid determination of
 734 biogenic opal in pelagic marine sediments. *Deep Sea Research Part A*.
 735 *Oceanographic Research Papers* **36**, 1415-1426 (1989).
 736 68. T. M. Conway, A. D. Rosenberg, J. F. Adkins, S. G. John, A new method for precise
 737 determination of iron, zinc and cadmium stable isotope ratios in seawater by double-
 738 spike mass spectrometry. *Analytica Chimica Acta* **793**, 44-52 (2013).
 739 69. T. M. Conway, S. G. John, F. Lacan, Intercomparison of dissolved iron isotope
 740 profiles from reoccupation of three GEOTRACES stations in the Atlantic Ocean.
 741 *Marine Chemistry* **183**, 50-61 (2016).
 742 70. C. M. Johnson, E. E. Roden, S. A. Welch, B. L. Beard, Experimental constraints on
 743 Fe isotope fractionation during magnetite and Fe carbonate formation coupled to
 744 dissimilatory hydrous ferric oxide reduction. *Geochimica et Cosmochimica Acta* **69**,
 745 963-993 (2005).

746

747

748 **Figure legends.**

749

750 **Figure 1. The location and core-top composition of sediment samples from GA10W.** A
 751 blue colour index shows 500 m water depth intervals in a plan view (top) of the study region
 752 and a section view (bottom) along the GA10W sample transect. Sediment classifications of
 753 stations 8-23 include cohesive silts-clays, whereas station 24 is a non-cohesive permeable sand.
 754 Station 18 lies well beneath the likely Carbonate Compensation Depth (CCD). Pie charts
 755 indicate the mean surface (0-5 cmbs) proportions of lithogenic and pelagic components between
 756 all sites (SI Appendix, Tables S1 and S2).

757

758 **Figure 2. (a) Porewater concentrations of dFe verses cFe.** Error bars ($\pm 2\sigma$) are typically
 759 within the size of individual data markers. Discrete observations from oxic-nitrogenous zones
 760 fall along a 1:1 line due to the high relative abundance of cFe. dFe exceeds cFe concentrations
 761 in underlying ferruginous zones due to the low relative abundance of cFe in these regions of
 762 the sediment. Concentrations of cFe span 3 orders of magnitude in porewater oxic-nitrogenous
 763 zones across all sites and exceed the concentrations of ocean bottom water (24), **(b) Mean**
 764 **porewater cFe concentration verses mean total organic carbon (TOC) in core top**
 765 **sediments (0-5cmbsf).** A dashed black line shows a significant linear fit through GA10W sites
 766 ($r = 0.962$, $p = 0.038$). Values from mafic volcanic sediments in the Southern Ocean (28),
 767 indicate that additional factors other than TOC also control the abundance of cFe in porewater,
 768 such as lithogenic provenance.

769

770 **Figure 3. The relationship between $\delta^{56}\text{dFe}$ and relative abundance of cFe in ocean**
 771 **sediment porewater.** Values compiled from the South Atlantic (this study sites 18, 21 and 22),
 772 and previous studies by (a) Homoky *et al.* (6) and (b) Klar *et al.* (7). Error bars ($\pm 2\sigma$) are
 773 within the size of individual data markers. The grey bar indicates the average Fe isotopic
 774 composition of crustal rocks.

775

776 **Figure 4. Modelled porewater Fe production rate profiles.** Comparison of measured sFe and
777 dFe with REC model fits to observations across the oxic/nitrogenous-ferruginous transition of
778 GA10W station 21. The concentrations and production rates of cFe are calculated by model
779 difference ($cFe = dFe - sFe$).

780

781 **Figure 5. Porewater sFe and cFe isotope mass-balance experiments.** Summary of results in
782 which porewater dFe isotope compositions are simulated by two idealised controls on the sFe
783 and cFe isotope reservoirs: Firstly, the isotope fraction effect (α) attributed to sFe loss (e.g.
784 oxidation), and secondly, the origin of porewater cFe. The value of α is either >1 (a, c) as is
785 commonly predicted for Fe(oxyhydr)oxide formation or <1 (b, d), as has been attributed to Fe
786 (oxyhydr)oxide formation across some ocean chemoclines (15) and is predicted by some other
787 (e.g. carbonate) mineral formations (70) and Fe(III)-ligand complexes (26). cFe is either an
788 authigenic mineral supplied by sFe oxidation with a corresponding isotope composition (a, b),
789 or cFe is supplied by non-reductive weathering of lithogenic material with crustal isotope
790 compositions (c, d). In all scenarios, the resultant composition of dFe reflects the isotopic mass
791 balance of sFe and cFe pools. Model equations are provided in the SI Appendix (SI Appendix,
792 SI Text 1).

793

794 **Figure 6. A revised scheme of sedimentary iron supply depicting seven processes that may**
795 **promote the exchange of lithogenic iron colloids (cFe) and isotopes to ocean interior.** (1)
796 Production and diffusion of lithogenic cFe (depicted as $cFeOOH(orgC)$) in oxic-nitrogenous
797 ocean sediment porewater; (2) Enhanced cFe production from dissolution of mafic minerals;
798 (3) Enhanced cFe stabilisation by organic C; (4) Porewater advection through permeable
799 sediments of the continental shelf; (5) Entrainment by internal waves and density horizons; (6)
800 Entrainments by a Benthic Boundary Layer (BBL) coupled to surface ocean EKE; (7)
801 Entrainment by the Surface Mixed Layer (SML) and Island Mass Effects. Sedimentary release
802 by reductive dissolution is restricted to shoaled porewater ferriclines beneath high organic
803 matter flux or Oxygen Minimum Zones (OMZs) in the upper 1500m of the ocean, and rely on
804 stabilisation by organic Ligands to resist secondary oxidation and precipitation from the water
805 column.

806

807 **Figure 7. (a) The isotopic signature of dissolved Fe in surface exchangeable sediment**
808 **porewaters.** Data markers correspond to measured surface values compiled from this study (SI
809 Appendix, Table S5), the South Atlantic, Cape margin (9), the North Pacific, Oregon and
810 California margins and Borderland Basins (6, 11), the North Atlantic, Celtic Sea (7), and the
811 Southern Ocean, Crozet Island abyss (6). The measured surface inventory of porewater dFe is
812 illustrated by the size of data markers, and the associated benthic flux (sediment consumption)
813 of O_2 by the colour scale. **(b) The entrainment potential for colloidal Fe and lithogenic**
814 **isotope signatures in the ocean.** Mean sediment community O_2 consumption rates compiled
815 by Stratmann *et al.* (65) are gridded here at 2 degrees and plotted using the same colour scale
816 to data in (a). The suspended particle load in bottom waters reported by Gardner *et al.* (29) is
817 reproduced with interpolated lines of equal concentration using means values from a 2-degree
818 grid.

819

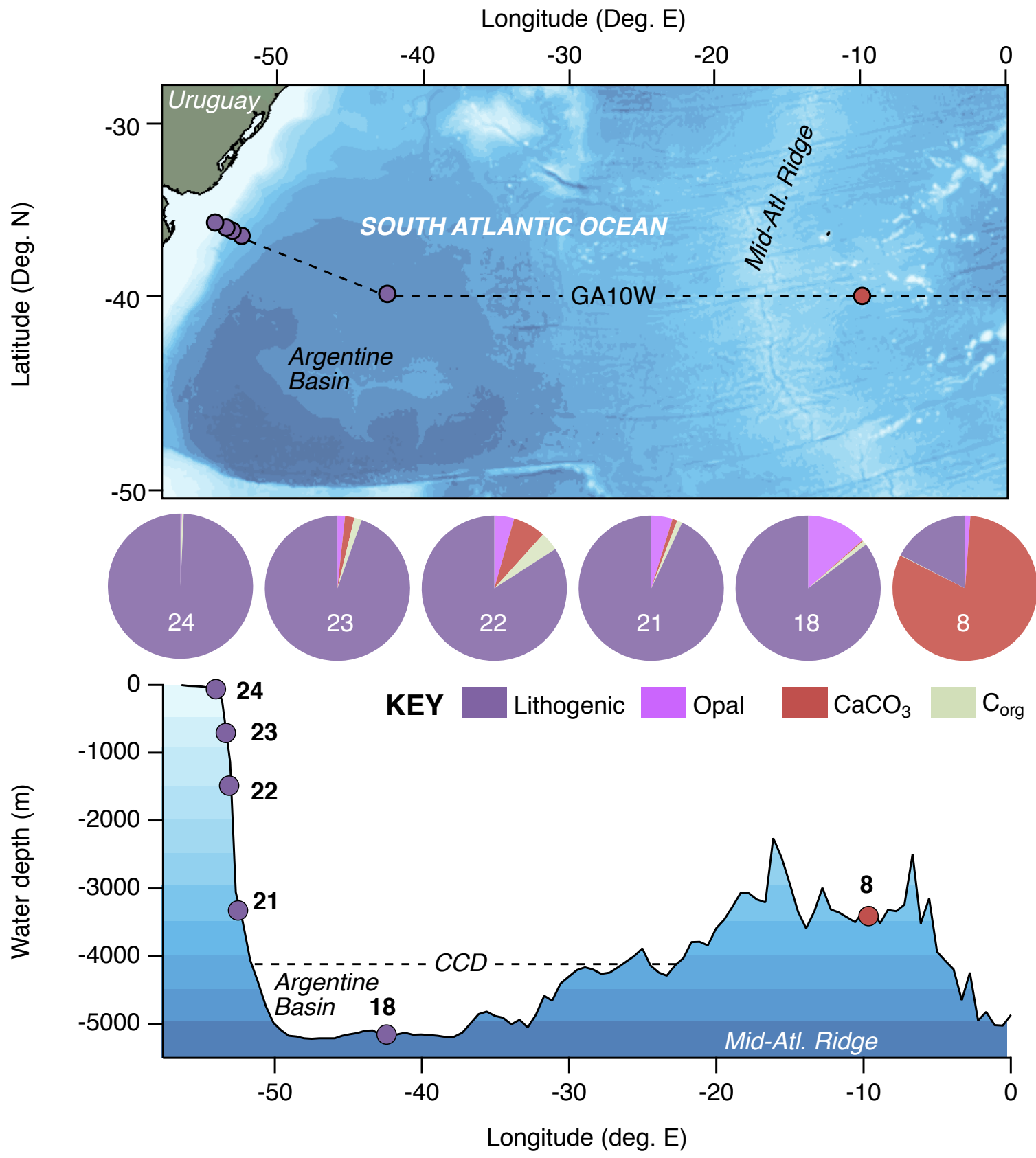


Figure 1

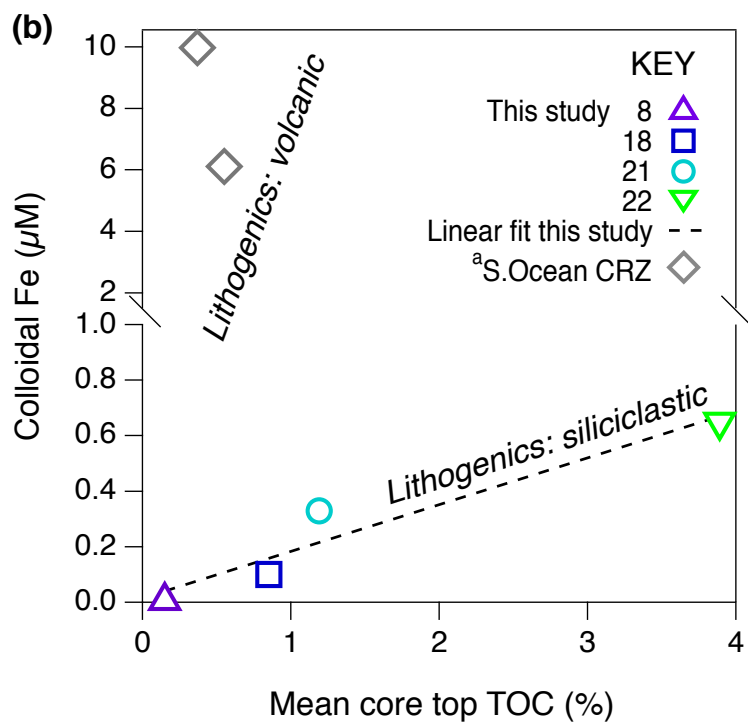
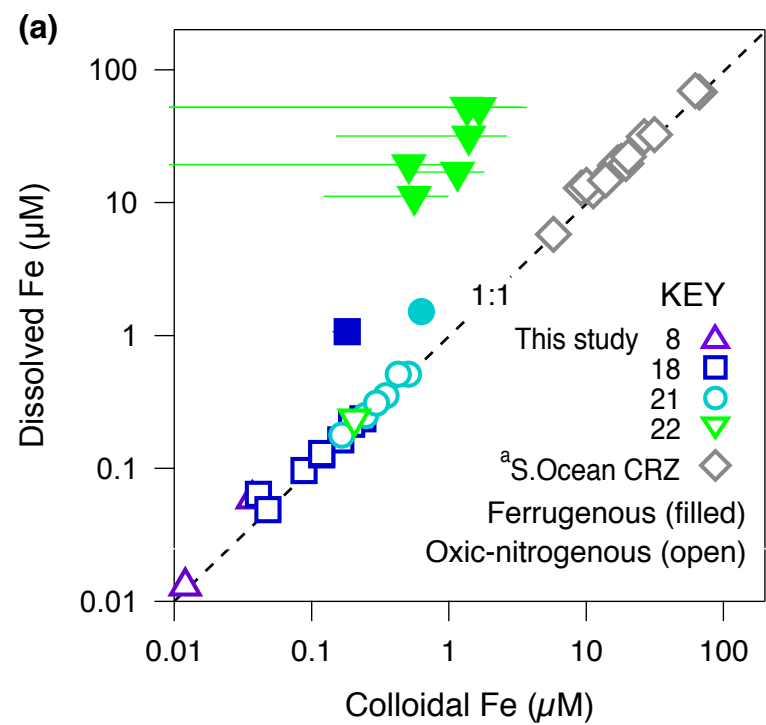


Figure 2

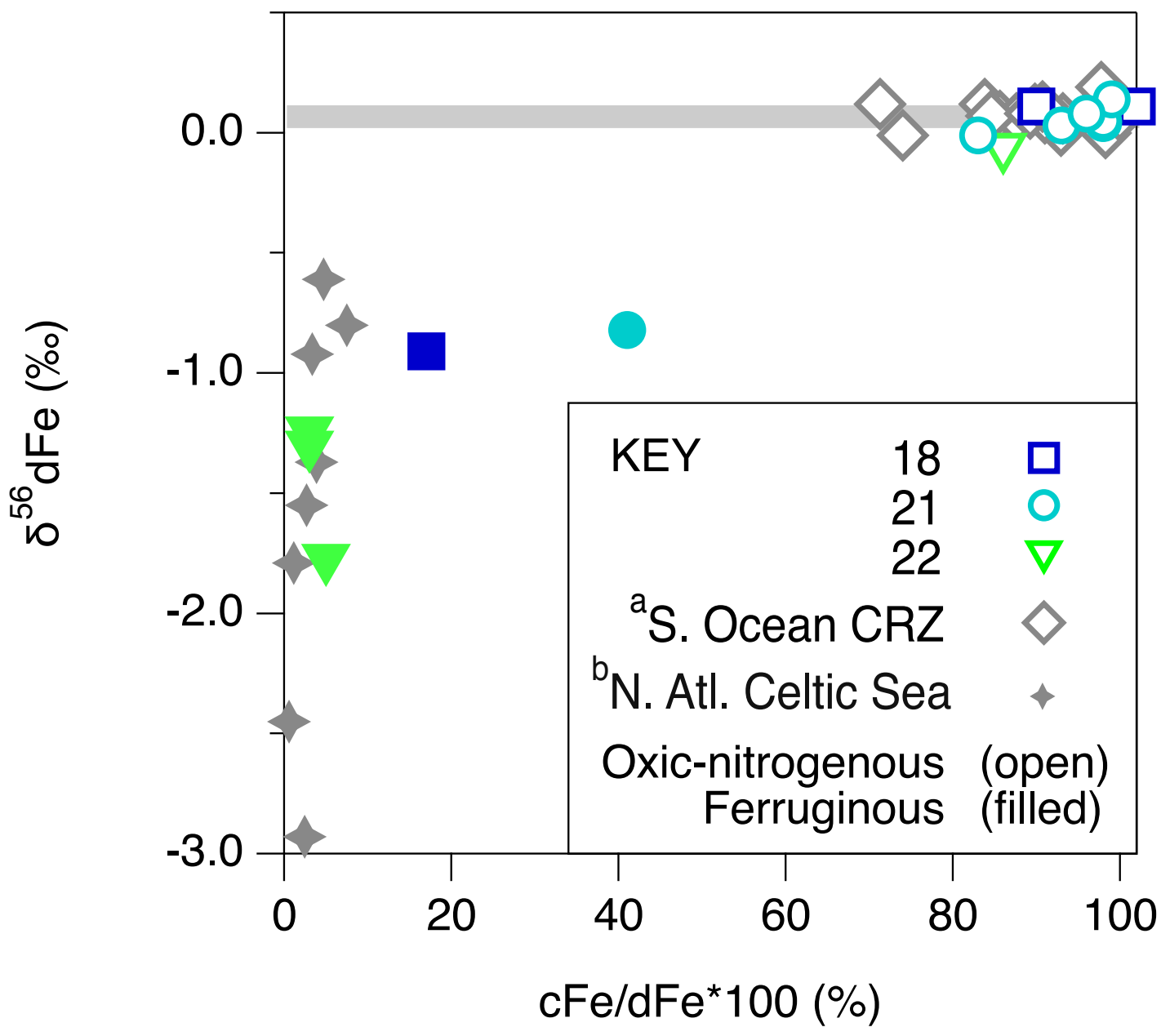
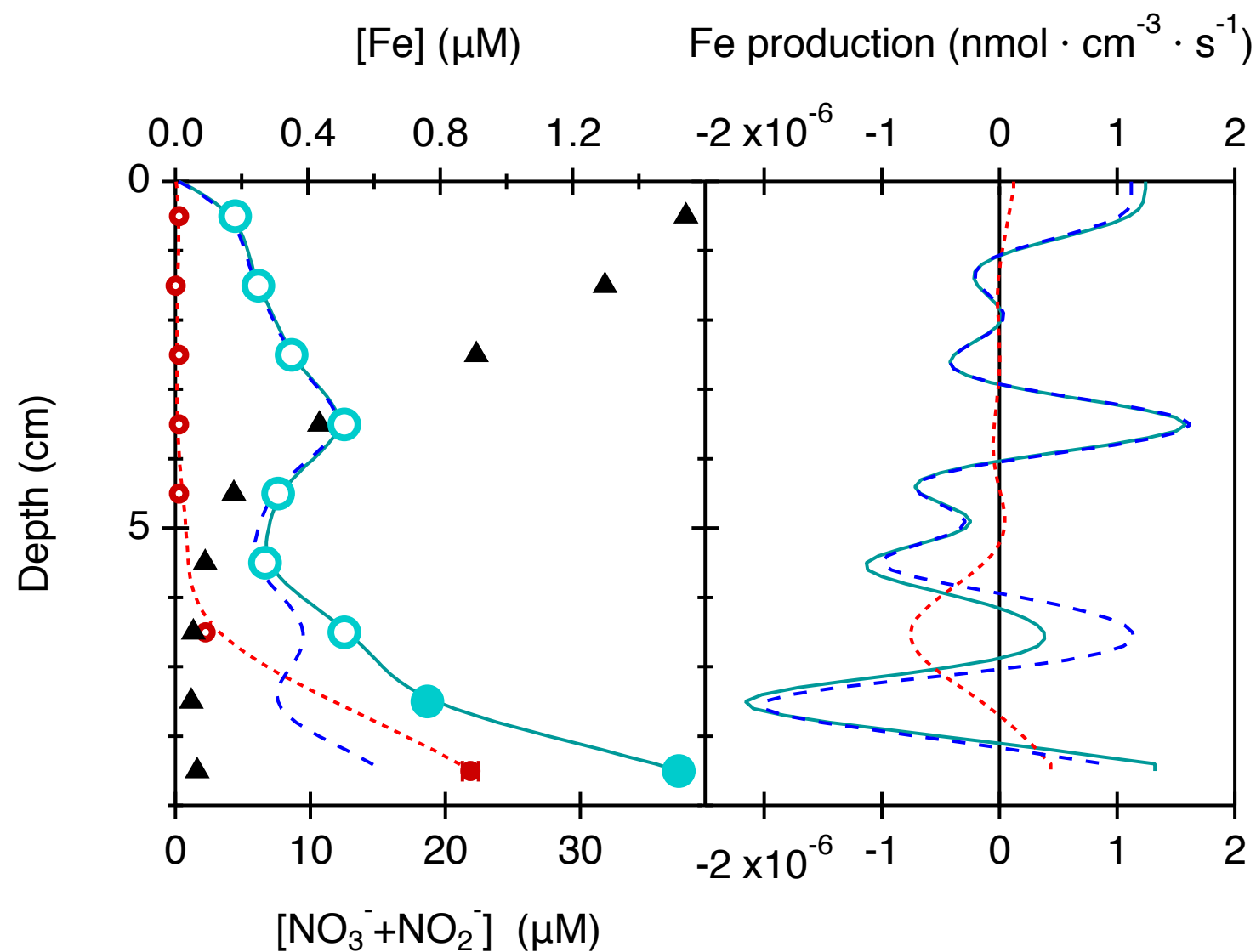


Figure 3



KEY		Obs.	Model
\blacktriangle	NO_x	\blacktriangle	
\bullet	sFe	\bullet	-----
\circ	cFe	\circ	- - - - -
\bullet	dFe	\bullet	—————
\circ	Oxic-Nitrogenous zone		
\bullet	Ferruginous zone		

Figure 4

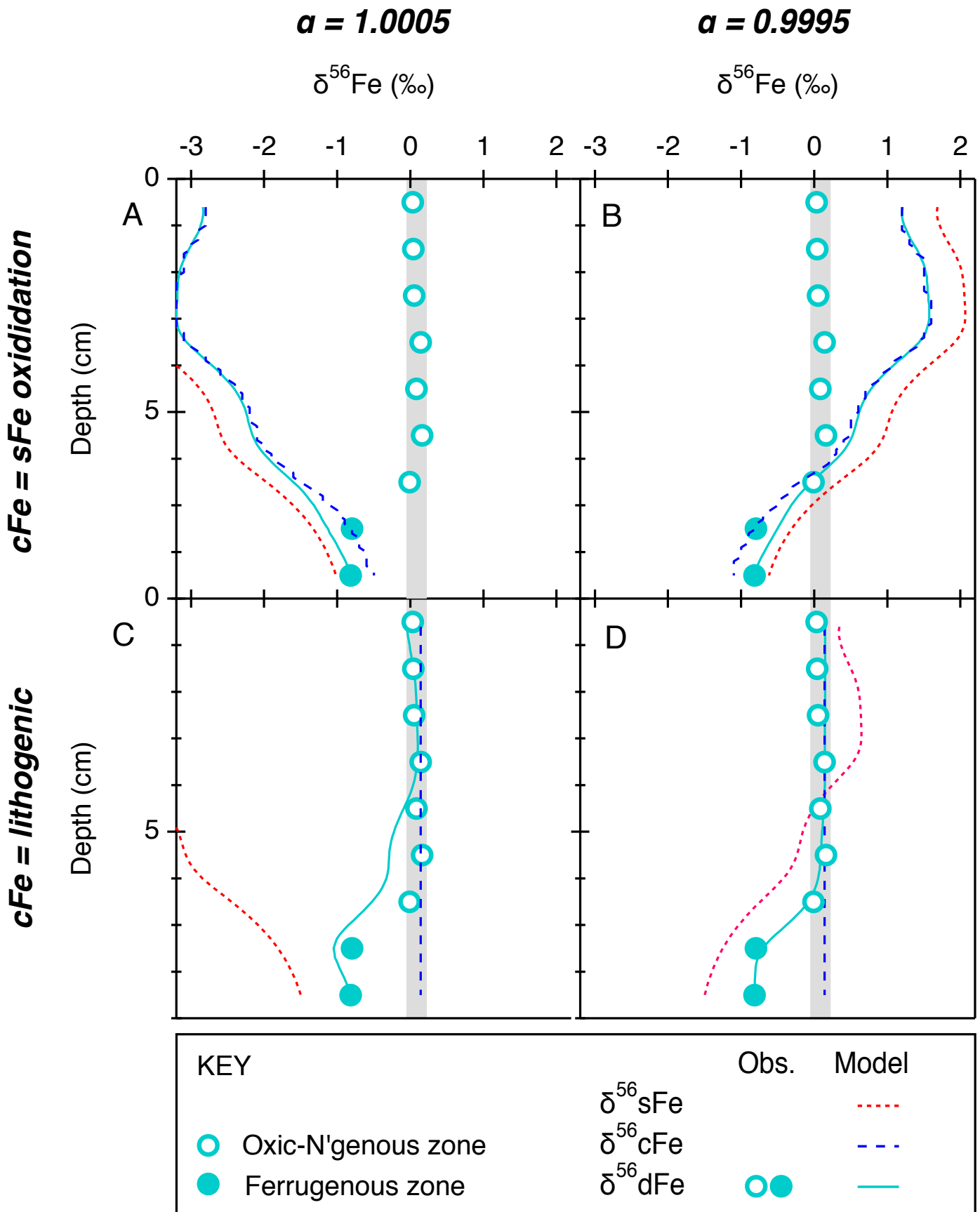


Figure 5

Lithogenic iron colloid production and supply to the ocean interior





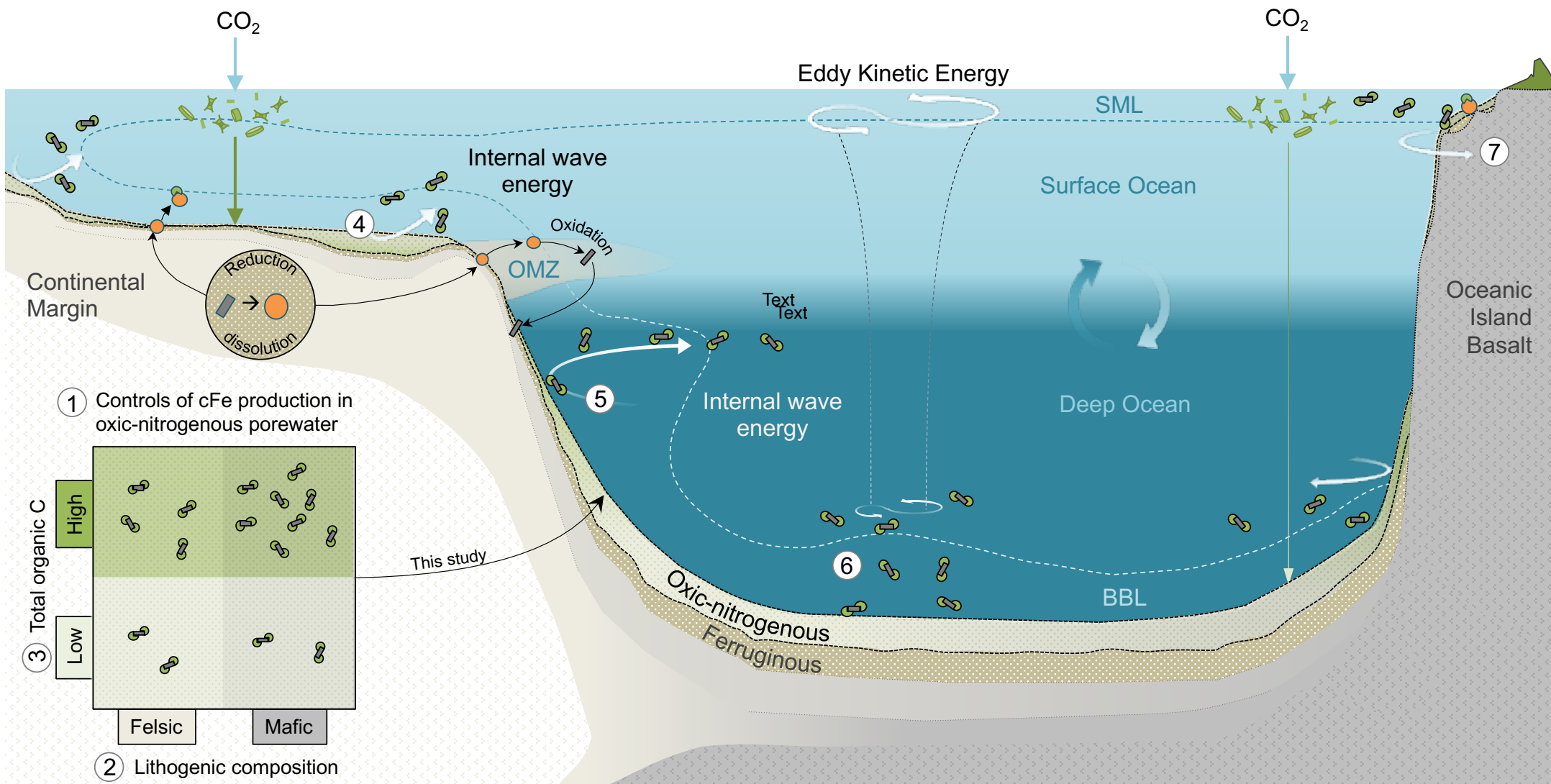
- KEY**
-  cFeOOH(orgC)
 -  FeOOH
 -  sFe(II)
 -  sFe(II/III)-L

Figure 6



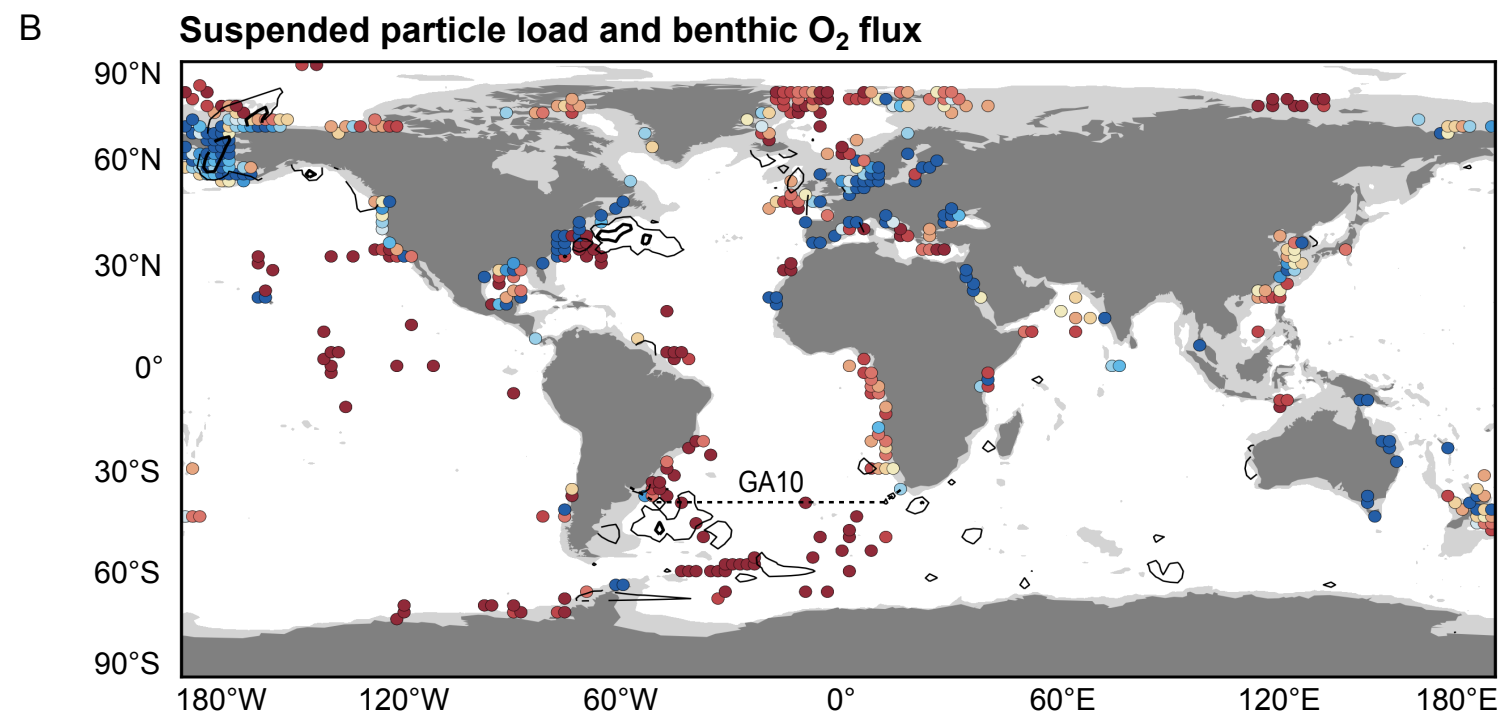
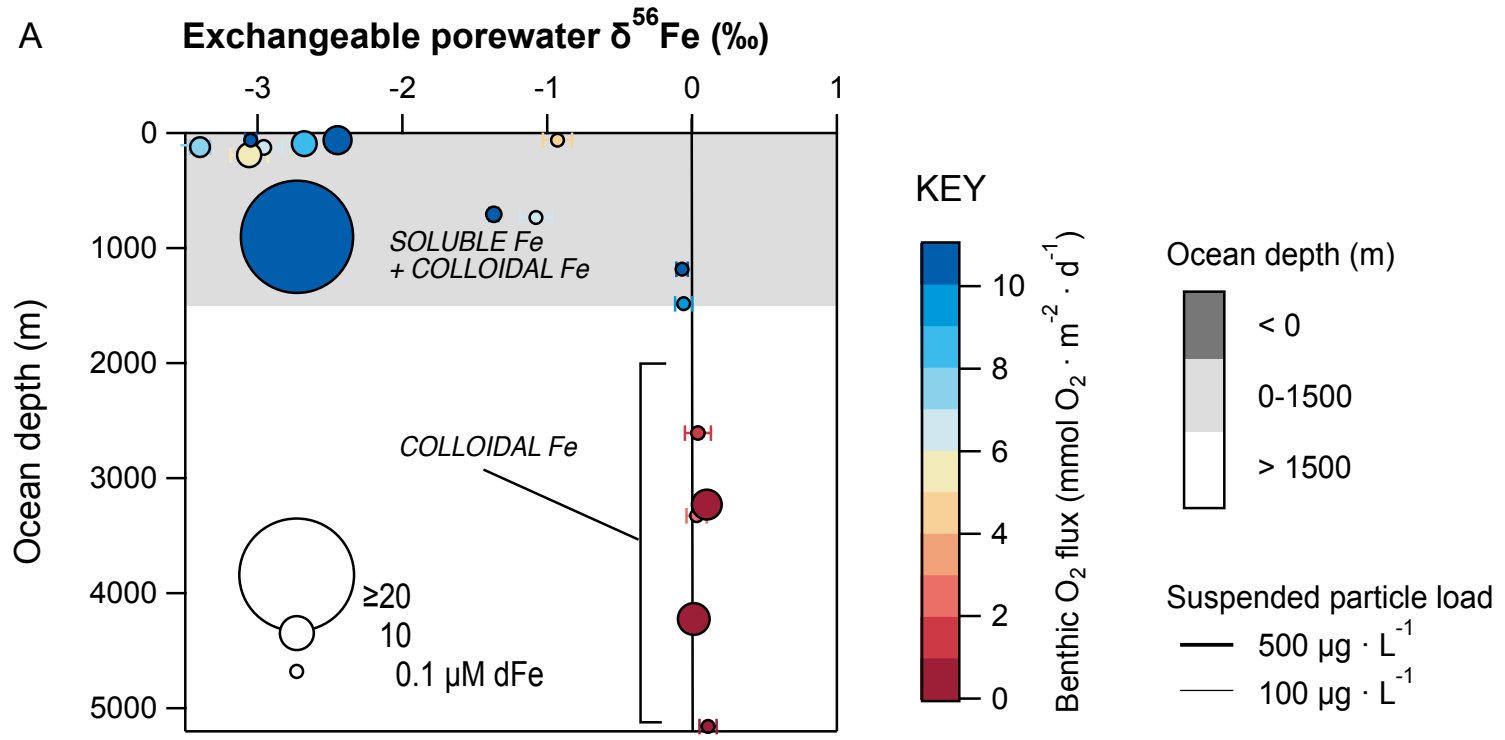


Figure 7